Insights into the mixing efficiency of submesoscale Centrifugal-Symmetric instabilities

Tomas Chor[a] , Jacob O. Wenegrat[a] , John Taylor[b]

[a] *Department of Atmospheric and Oceanic Science, University of Maryland, College Park, MD*

[b] *Department of Applied Mathematics and Theoretical Physics, University of Cambridge, Cambridge, United Kingdom*

Corresponding author: Tomas Chor, tchor@umd.edu

ABSTRACT: Submesoscale processes provide a pathway for energy to transfer from the balanced circulation to turbulent dissipation. One class of submesoscale phenomena that has been shown to be particularly effective at removing energy from the balanced flow are centrifugal-symmetric instabilities (CSIs), which grow via geostrophic shear production. CSIs have been observed to generate significant mixing in both the surface boundary layer and bottom boundary layer flows along bathymetry, where they have been implicated in the mixing and watermass transformation of Antarctic Bottom Water. However, the mixing efficiency (i.e. the fraction of the energy extracted from the flow used to irreversibly mix the fluid) of these instabilities remains uncertain, making estimates of mixing and energy dissipation due to CSI difficult.

In this work we use large-eddy simulations to investigate the mixing efficiency of CSIs in the submesoscale range. We find that centrifugally-dominated CSIs (i.e. CSI mostly driven by horizontal shear production) tend to have a higher mixing efficiency than symmetrically-dominated ones (i.e. driven by vertical shear production). The mixing efficiency associated with CSIs can therefore alternately be significantly higher or significantly lower than the canonical value used by most studies. These results can be understood in light of recent work on stratified turbulence, whereby CSIs control the background state of the flow in which smaller-scale secondary overturning instabilities develop, thus actively modifying the characteristics of mixing by Kelvin-Helmholtz instabilities. Our results also suggest that it may be possible to predict the mixing efficiency with more readily measurable parameters (namely the Richardson and Rossby numbers), which would allow for parameterization of this effect.

1. Introduction

Submesoscale currents (roughly defined as having horizontal scales between 0.1–10 km) are common in oceanic flows, with significant impacts on global ocean dynamics (McWilliams 2016; Lévy et al. 2018; Garabato et al. 2019; Buckingham et al. 2019; Wenegrat et al. 2018b). In particular they are understood to be one of the major pathways for energy in the large scales of the ocean to cascade down to the smallest scales of the flow — a necessary condition for that energy to be dissipated and consequently for the approximate steady-state of the ocean circulation to be achieved (McWilliams 2016).

Recent work has highlighted centrifugal-symmetric instabilities (CSIs) as particularly effective at generating this forward cascade (D'Asaro et al. 2011; Gula et al. 2016b). These instabilities are active both at the surface (Taylor and Ferrari 2010; D'Asaro et al. 2011; Thomas et al. 2013; Gula et al. 2016a; Savelyev et al. 2018) and in the bottom boundary layer and topographic wakes (Allen and Newberger 1998; Dewar et al. 2015; Molemaker et al. 2015; Gula et al. 2016b; Garabato et al. 2019; Wenegrat et al. 2018a; Wenegrat and Thomas 2020) and, as such, they may be important both for the energetics of global circulation, as well as for the mixing of buoyancy and other tracers. As an example, it has been suggested that mixing by CSIs may lead to significant watermass transformation of Antarctic Bottom Water, possibly affecting the closure of the abyssal overturning circulation (Garabato et al. 2019; Spingys et al. 2021). However, despite evidence of their potential impacts, the characteristics and dynamics of mixing by submesoscale CSIs remain uncertain. Thus, we dedicate this study to the investigation of this topic.

A common measure of a flow's mixing is given by its mixing efficiency γ, which measures the fraction of the energy extracted from the flow that was used to mix the fluid's buoyancy. The value of γ is bounded between 0 and 1 and is generally assumed to be $\gamma \approx 0.17$ for ocean turbulence (Osborn 1980; Moum 1996; Wunsch and Ferrari 2004; Bluteau et al. 2013; De Lavergne et al. 2016; Mashayek et al. 2017b) which, historically, has fit most measured ocean data reasonably well (Gregg et al. 2018). However, recent investigations have hinted at γ varying widely due to submesoscale phenomena. Notably, a recent field study conducted in the Orkney Deep (Spingys et al. 2021) inferred significantly higher mixing efficiencies (with an average value of $\gamma = 0.48$) in a location that is likely unstable to CSIs (Garabato et al. 2019). Numerical simulations by Jiao and Dewar (2015) likewise indicated values of $\gamma > 0.3$, with speculations that the value could be larger if the simulation was run for longer. These results seem to contrast with those by Taylor and Ferrari (2010), which found some forms of CSI are associated with small time- and spatially-integrated vertical buoyancy production rates, suggesting small rates of irreversible mixing of buoyancy (Peltier and Caulfield 2003; Caulfield 2021).

With these ideas in mind, we investigate the mixing efficiency of submesoscale CSIs (Haine and Marshall 1998) using large-eddy simulations (LES) of finite-width geophysical set-ups. This configuration aims to reproduce the natural constraints of oceanic flows (due to rotation, natural forcing patterns, etc.) and to obtain somewhat realistic flow evolution and mixing dynamics. This is in contrast to previous numerical studies with similar lines of investigation, which used more highly idealized set-ups (Maffioli et al. 2016; Garanaik and Venayagamoorthy 2019; Howland et al. 2020) or employed assumptions which can potentially affect mixing patterns (e.g. assuming an infinite-width front (Thomas et al. 2013; Taylor and Ferrari 2010) or a two-dimensional flow (Jiao and Dewar 2015)).

We show evidence that, in the submesoscale range of the parameter space, CSIs equilibrate via secondary Kelvin-Helmholtz instabilities. This fact allows us to make direct connections with the literature on the mixing efficiency of turbulence in stratified flows, which provides a framework for explaining the range of mixing efficiencies generated by CSIs. In short, CSIs control the flow's mixing efficiency by modulating the background state for the secondary Kelvin-Helmholtz instabilities, which overturn and create the smaller-scale 3D turbulent motions that ultimately dissipate kinetic energy and mix buoyancy. The result of this cascade is that mixing is more efficient for CSIs dominated by centrifugal modes (i.e. mostly driven by horizontal shear production) and less efficient for symmetrically-dominated ones (i.e. driven by vertical shear production).

2. Theoretical background

A brief review of CSIs and mixing efficiencies follows and the reader is directed other to works for further details (Haine and Marshall 1998; Bluteau et al. 2013; Gregg et al. 2018; Caulfield 2021).

a. CSI theory

Centrifugal-symmetric instabilities (CSIs; sometimes referred to simply as symmetric instabilities) are defined here are those which emerge when $qf < 0$ (Haine and Marshall 1998). Here f is the Coriolis frequency and q is the Ertel potential vorticity (PV):

$$q = \nabla b \cdot (\nabla \times \boldsymbol{u} + f\hat{\boldsymbol{k}}), \tag{1}$$

where ∇ is the gradient operator, b is the buoyancy, $\boldsymbol{u}$ is the velocity vector and $\hat{\boldsymbol{k}}$ is the unit vector in the vertical (z) direction. When the flow is in thermal wind balance Equation (1) can be re-written as

$$\hat{q}_b = 1 + Ro_b - \frac{1}{Ri_b}, \tag{2}$$

where $\hat{q}_b = q/N^2 f$ is the normalized PV, $N = \sqrt{db/dz}$ is the Brunt-Vaisala frequency, $Ro_b = \zeta_b/f$ is the balanced Rossby number, ζ_b is the vertical vorticity, $Ri_b = N^2/|d\boldsymbol{u}_b/dz|^2$ is the Richardson number and $\boldsymbol{u}_b$ is the (horizontal) velocity component in thermal wind balance. (The subscript b is used to indicate an assumption of thermal wind balance throughout this paper.) This essentially reduces the instability criterion to $\hat{q}_b < 0$. Given the dynamical definition of the submesoscale range as $Ro \sim Ri \approx 1$, it can be seen from Equation (2) that CSIs can be active for many submesoscale flows.

It is useful to characterize CSIs based on their primary source of kinetic energy (Thomas et al. 2013). For the purposes of this paper we focus on the horizontal shear production rates ($\langle SP_h \rangle$, associated with the centrifugal modes; $\langle \cdot \rangle$ denotes a volume average) and vertical shear production rates ($\langle SP_v \rangle$, associated with symmetric modes). Hence, a straightforward way to characterize CSIs is by estimating their ratio, which (assuming a background flow with uniform gradients, and that CSI-unstable parcels move in paths whose angle with the horizontal direction is small) can approximated as (Thomas et al. 2013, Equation (42))

$$\frac{\langle SP_h \rangle}{\langle SP_v \rangle} = R_{\mathrm{SP}} \approx -Ro_b\, Ri_b \left(1 - \frac{f^2}{N^2}(1 + Ro_b)\right), \tag{3}$$

where R_{SP} is the ratio of horizontal to vertical shear production rates. Thus the larger R_{SP}, the more centrifugally-dominated a CSI (and opposite for symmetrically-dominated CSIs). In all cases in this paper the second term in parenthesis is small and we approximate Equation (3) by

$$R_{\mathrm{SP}} \approx -Ro_b\, Ri_b, \tag{4}$$

which can be understood as the ratio of the two non-unitary terms in Equation (2). Hence, whenever $\hat{q}_b$ is negative due primarily to Ro_b being sufficiently negative (i.e. due to the horizontal shear), we call the ensuing instability a centrifugally-dominated CSI ($R_{\mathrm{SP}} > 1$). Similarly, when $\hat{q}_b < 0$ due to Ri_b being small (i.e. due to the vertical shear), we say the ensuing instability is symmetrically-dominated ($R_{\mathrm{SP}} < 1$).

We note that, while CSIs are generally understood to grow using the kinetic energy of the balanced flow through the shear production rate terms (Haine and Marshall 1998), Wienkers et al. (2021) showed that in the limiting case of $Ro_b = 0$ and for fronts with relatively shallow isopycnal slopes, symmetrically-dominated CSIs can grow primarily at the expense of the potential energy of the balanced flow, making the vertical buoyancy flux term dominant. Although these limiting cases may be relevant for some broad fronts, we do not focus on this part of the parameter space in this study.

In the general case (a CSI where both or either Ro_b and Ri_b contribute to $\hat{q}_b$ being negative), and again assuming a balanced background flow, the linear inviscid growth rate ω of the instability is (Haine and Marshall 1998)

$$\omega^2 \leq -f^2 \hat{q}_b, \tag{5}$$

which reveals that, at a fixed latitude, a given CSI will grow faster the more negative $\hat{q}_b$ is.

b. Mixing efficiency theory

We focus on the mixing efficiency γ, which we define as

$$\gamma(t) = \frac{\langle \varepsilon_p \rangle}{\langle \varepsilon_p \rangle + \langle \varepsilon_k \rangle}, \tag{6}$$

where ε_k is kinetic energy dissipation rate and ε_p is the rate of irreversible mixing of buoyancy. Note that there are many definitions of γ in the literature (see Gregg et al. (2018) for a review), but we choose Equation (6) because it specifically considers only irreversible processes, making it more accurate. We also consider the cumulative mixing efficiency (Gregg et al. 2018; Caulfield 2021):

$$\Gamma(t) = \frac{\int_0^t \langle \varepsilon_p \rangle \, dt'}{\int_0^t \left[\langle \varepsilon_p \rangle + \langle \varepsilon_k \rangle \right] \, dt'}. \tag{7}$$

Since both $\langle \varepsilon_k \rangle$ and $\langle \varepsilon_p \rangle$ eventually go to zero after a sufficiently long time, $\Gamma(t)$ approaches an asymptotic value as $t \to \infty$. This makes Γ a better approach to quantify the cumulative mixing of a given instability over its lifetime.

Dimensional analysis indicates that the mixing efficiency (either γ or Γ) of a given flow depends on several parameters, albeit it remains unclear which ones are the most important or what is the functional shape of these dependencies (Caulfield 2021). One potentially important parameter is the buoyancy Reynolds number (Shih et al. 2005), which, based on recent literature, seems to organize results from idealized numerical simulations reasonably well (Shih et al. 2005; Bouffard and Boegman 2013; Salehipour and Peltier 2015). It was proposed in part because it is easier to estimate in field campaigns than a more traditional Reynolds number, serving as a proxy for the intensity of turbulence. It can be written as

$$Re_b = \frac{\langle \varepsilon_k \rangle}{\nu_{\text{mol}} N_0^2}, \tag{8}$$

where N_0^2 is a constant background stratification and ν_{mol} is the molecular viscosity of the fluid.

3. Problem set-up

We use a numerical setup that approximates geophysical flows while allowing the Rossby and Richardson numbers of the flow to be easily varied. In this section we describe that setup in detail, including the numerical tools used for the simulations.

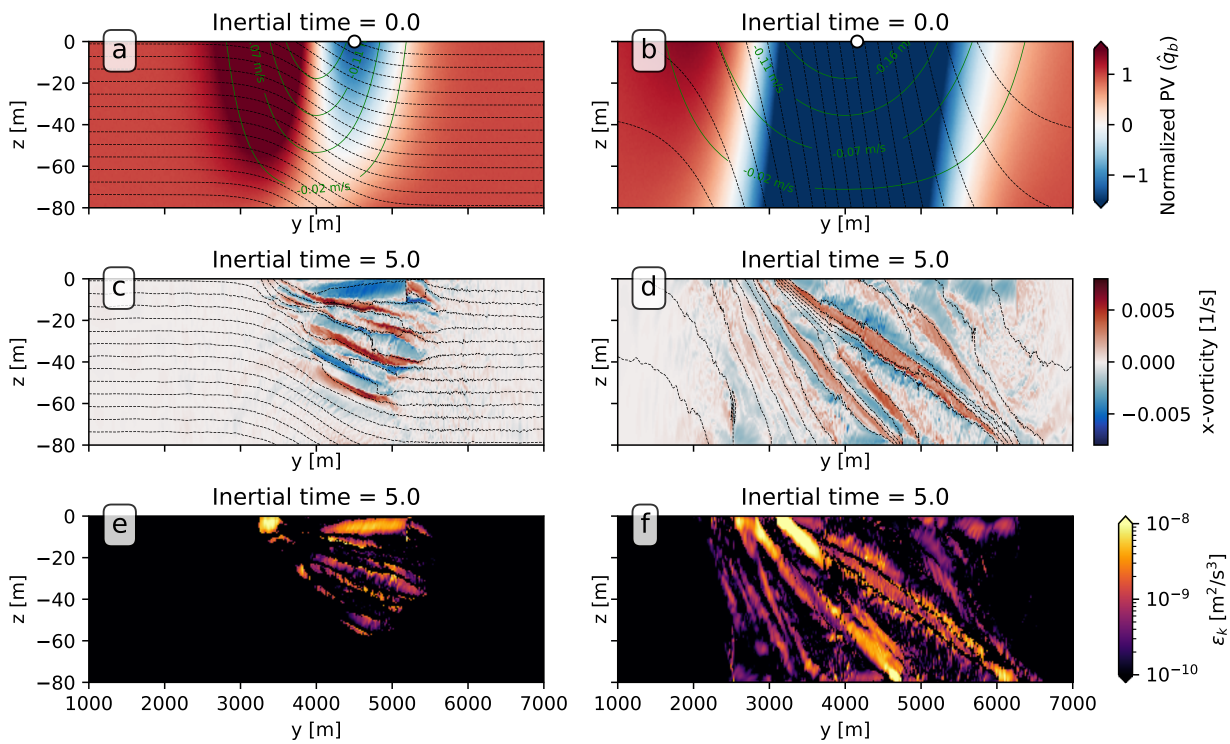

FIG. 1. Vertical cross-sections of two simulations used in this work — CIfront1 (panels a, c and e) and SIfront4 (panel b, d and f), described in detail in Section b. Dashed black lines show isopycnals, green lines are contours of constant u-velocity. Upper panels (a and b) show the normalized PV $\hat{q}_b$ in the initial condition, middle panels (c and d) show the x-component of the vorticity vector at around 5 inertial periods (after the onset of 3D turbulence), and lower panels (e and f) show the instantaneous dissipation rate ε_k. Animations for these simulations are also available in the Supporting Information.

a. Initial conditions

We start our simulations with a thermal-wind-balanced front configuration given by the following equations:

$$v = w = 0, \tag{9}$$

$$u = u_0 \, f_y(y) \, f_z(z), \tag{10}$$

$$b = -u_0 f_0 \, F_y(y) \frac{df_z(z)}{dz} + N_0^2 z, \tag{11}$$

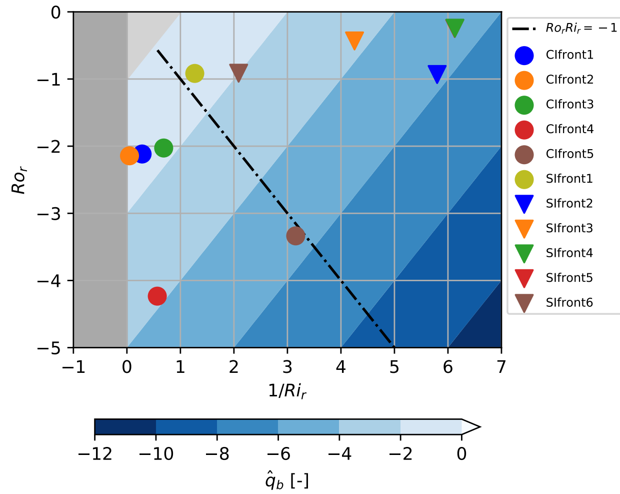

FIG. 2. Simulations (circles and triangles) on top of the Ro_r-$1/Ri_r$ parameter space. The dark gray areas denote regions of negative Ri_r (thus impossible to achieve in a stably stratified environment such as ours) and light gray areas denote regions stable to CSIs ($\hat{q}_b > 0$). Dot-dashed line corresponds to $Ro_r Ri_r = -1$, which theoretically separates centrifugally-dominated (to the left of the line) from symmetrically-dominated CSIs (to the right of the line) for a thermal-wind-balanced environment. Note that Simulation SIfront5 does not appear in the plot but is located at the same point as Simulation SIfront4.

where u_0 is a velocity constant. f_y, F_y and f_z are nondimensional functions of y and z given by

$$f_y(y) = \exp\left(-\frac{(y-y_0)^2}{\sigma_y^2}\right), \tag{12}$$

$$F_y(y) = \int_{-\infty}^{y} f_y(y')dy' = \frac{1}{2}\sqrt{\pi}\sigma_y\left[\mathrm{erf}\left(\frac{y-y_0}{\sigma_y}\right)+1\right], \tag{13}$$

$$f_z(z) = \frac{z-z_0}{\sigma_z}+1, \tag{14}$$

where, for the purposes of our paper $z_0 = 0$, $\sigma_z = 80$, and y_0 is always set to be half the length of our domain in the y direction (4 km; see Section b).

The equations above define a Gaussian-shaped front centered at y_0 with a vertically-constant vertical shear of u_0/σ_z, a width σ_y, and a superimposed spatially-uniform background stratification N_0^2. A vertical cross-section of the front showing $\hat{q}_b$ can be seen in the top panels of Figure 1 for two different sets of parameters (details are given in Section b). Recall that CSIs emerge in the regions where $\hat{q}_b$ (shown in the color map) is negative.

Table 1. Parameters for the main simulations used in this paper. All simulations have vertical length scales $\sigma_z = 80\,\mathrm{m}$, domain lengths $L_x = 500\,\mathrm{m}$, $L_y = 8000\,\mathrm{m}$ and $L_z = 80\,\mathrm{m}$ with grid spacings $\Delta x = \Delta y = 2.5\,\mathrm{m}$ and $\Delta z = 0.625\,\mathrm{m}$.

Simulation	σ_y (m)	f (1/s)	u_0 (m/s)	N_0^2 (1/s^2)	Ro_r	Ri_r	δ	Γ_∞
CIsurfjet1	800	1.0×10^{-4}	-2.0×10^{-1}	1.0×10^{-5}	−2.1	3.5	1.00×10^{-1}	0.21
CIsurfjet2	800	1.0×10^{-4}	-2.0×10^{-1}	5.0×10^{-5}	−2.1	20.8	1.00×10^{-1}	0.24
CIsurfjet3	800	1.0×10^{-4}	-2.0×10^{-1}	5.0×10^{-6}	−2.0	1.5	1.00×10^{-1}	0.27
CIsurfjet4	800	5.0×10^{-5}	-2.0×10^{-1}	5.0×10^{-6}	−4.2	1.8	1.00×10^{-1}	0.21
CIsurfjet5	600	7.0×10^{-5}	-2.0×10^{-1}	1.4×10^{-6}	−3.3	0.3	1.33×10^{-1}	0.26
SIsurfjet1	1600	1.0×10^{-4}	-2.3×10^{-1}	5.0×10^{-6}	−0.9	0.8	5.00×10^{-2}	0.19
SIsurfjet2	800	1.0×10^{-4}	-2.0×10^{-1}	1.0×10^{-6}	−0.9	0.2	1.00×10^{-1}	0.13
SIsurfjet3	1400	1.0×10^{-4}	-2.0×10^{-1}	1.4×10^{-6}	−0.4	0.2	5.71×10^{-2}	0.12
SIsurfjet4	1600	1.0×10^{-4}	-2.0×10^{-1}	1.0×10^{-6}	−0.2	0.2	5.00×10^{-2}	0.11
SIsurfjet5	800	1.0×10^{-4}	-1.0×10^{-1}	2.5×10^{-7}	−0.2	0.2	1.00×10^{-1}	0.06
SIsurfjet6	1200	1.0×10^{-4}	-2.0×10^{-1}	2.5×10^{-6}	−0.9	0.5	6.67×10^{-2}	0.17

Table 2. Parameters for the auxiliary simulations used in this paper. All simulations have vertical length scales $\sigma_z = 80\,\mathrm{m}$, domain lengths $L_y = 8000\,\mathrm{m}$, $L_z = 80\,\mathrm{m}$, and grid spacings $\Delta y = \Delta z = 0.156\,\mathrm{m}$.

Simulation	σ_y (m)	f (1/s)	u_0 (m/s)	N_0^2 (1/s^2)	ν_e (m^2/s)	Ro_r	Ri_r	δ
2D_CIsurfjet1	800	1.0×10^{-4}	-2.0×10^{-1}	1.0×10^{-5}	5.0×10^{-4}	−2.1	3.5	1.00×10^{-1}
2D_CIsurfjet3	800	1.0×10^{-4}	-2.0×10^{-1}	5.0×10^{-6}	5.0×10^{-4}	−2.0	1.5	1.00×10^{-1}
2D_SIsurfjet4	1600	1.0×10^{-4}	-2.0×10^{-1}	1.0×10^{-6}	1.0×10^{-3}	−0.2	0.2	5.00×10^{-2}

Our set-up can be fully defined with the parameters u_0, σ_y, σ_z, N_0^2, f, the eddy viscosity ν_e, and the eddy diffusivity of buoyancy κ. Application of dimensional analysis produces five nondimensional parameters:

$$\delta = \frac{\sigma_z}{\sigma_y}, \tag{15}$$

$$Pr = \frac{\nu_e}{\kappa}, \tag{16}$$

in addition to Rossby, Richardson, and Reynolds numbers. Here δ is the aspect ratio and Pr is the Prandtl number. For simplicity we only consider the case $Pr = 1$ (which in our case is a turbulent Prandtl number since we use eddy diffusivity closures) and, given the uncertainty of δ in real oceanic conditions, we assume that the aspect ratio does not affect results as strongly as the Rossby or Richardson numbers. We thus report δ, but do not make efforts to explore its range.

In order to use representative values to characterize our simulations, we use Ro_r and Ri_r, which we refer to as reference Rossby and Richardson numbers, to characterize the parameter space. They are defined as the Rossby and Richardson numbers at the point of the domain where $\hat{q}_b$ is initially (i.e. at $t = 0$) the lowest. Recall that this corresponds to the point with the fastest linear growth rate for CSIs according to Equation (5), making Ro_r and Ri_r relevant quantities of the flow evolution. For our set-up, this point always lies at $z = 0$ but the y-location is found numerically given the challenge of obtaining a closed-form expression for it from Equations (9)-(14). The reference point is shown as white circles in Figure 1a-b. A parameter space of Ro_r-$1/Ri_r$ is shown in Figure 2, where the color map shows values of $\hat{q}_b$ at the reference point.

Finally, following previous literature (Shih et al. 2005; Salehipour and Peltier 2015), we use the buoyancy Reynolds number (properly defined for LES cases in Equation (17)) to diagnose the turbulence intensity related to the stabilizing effect of stratification. We focus our exploration of parameter space on the Rossby and Richardson numbers and we use the buoyancy Reynolds number as a diagnostic quantity.

b. Simulations

We use the Julia package Oceananigans (Ramadhan et al. 2020) to run a series of numerical simulations with Equations (9)–(14) as initial conditions. Oceananigans uses a finite volume discretization based on that of MITgcm (Marshall et al. 1997) and we run it with a 5th-order Weighted Essentially Non-Oscillatory advection scheme and a 3rd-order Runge-Kutta time-stepping method. The bulk of our simulations are three-dimensional (3D) LES (whose parameters can be found in Table 1), but we also run three auxiliary two-dimensional (2D) simulations with a constant eddy viscosity (whose purpose is made clear in Section 4 and whose parameters can be found in Table 2). The two-dimensional domains retain all three velocity components despite only formally including the y and z directions, in what is sometimes called 2.5D set-up (Kämpf 2010).

All simulations are bounded in the y and z directions, and the 3D simulations are periodic in the x (alongfront) direction. In all cases a buoyancy gradient of $db/dz = N_0^2$ was imposed at the top and bottom boundaries (in order to minimize initial dissipation of buoyancy before the onset of turbulence) and all other nonperiodic boundary conditions imposed zero fluxes for the momentum components and the buoyancy scalar. No-flux boundary conditions at the top and bottom of the domain were also tested and found to not affect our findings. A constant background rotation rate f was imposed on the domain for each simulation and sponge layers were included on both ends of the y direction with a width of 1/16th of the domain length each to absorb internal waves and simulate open boundaries.

For the 2D set-ups, a constant isotropic eddy diffusivity was used with its value set to be as low as possible while still producing well-resolved simulations. Resolvedness was verified both by inspecting the small scales of the flow visually and by ensuring that the Kolmogorov microscale $[(\nu_e^3/\varepsilon_k)^{1/4}]$ was always at least $\approx 30\%$ larger than the grid spacing (further refining produced no significant change in the results). In the 3D simulations we used a constant-coefficient Smagorinsky model closure (Smagorinsky 1963) with a modification that reduces the eddy viscosity in stably-stratified regions (Lilly 1962). We also ran a select number of 3D simulations with the anisotropic minimum dissipation subgrid scale closure (as implemented in Vreugdenhil and Taylor (2018)) and verified only small quantitative differences and identical qualitative behavior. Thus, only simulations with the Smagorinsky model are used in this manuscript.

The simulation parameters for the main (3D LES) runs are given in Table 1 and their location in the Ro_r-$1/Ri_r$ parameter space can be seen in Figure 2, where each symbol corresponds to a simulation. Relevant simulation parameters for the auxiliary 2D runs are given in Table 2. Their values for Ro_r and Ri_r are exactly the same as those of their 3D counterparts so they do not expand the exploration of the parameter space.

4. Results

a. Time evolution of the mixing efficiencies

All our simulations go through qualitatively similar evolutions: 2D primary instabilities (CSIs) develop quickly in the initially-unstable ($\hat{q}_b < 0$) region, followed by the sudden onset of the secondary instabilities creating 3D turbulence and releasing internal waves, followed by a longer decay of the turbulence. We focus for now on simulations CIfront1 and SIfront4 (representative of centrifugally- and symmetrically-dominated CSIs, respectively) to illustrate that process in

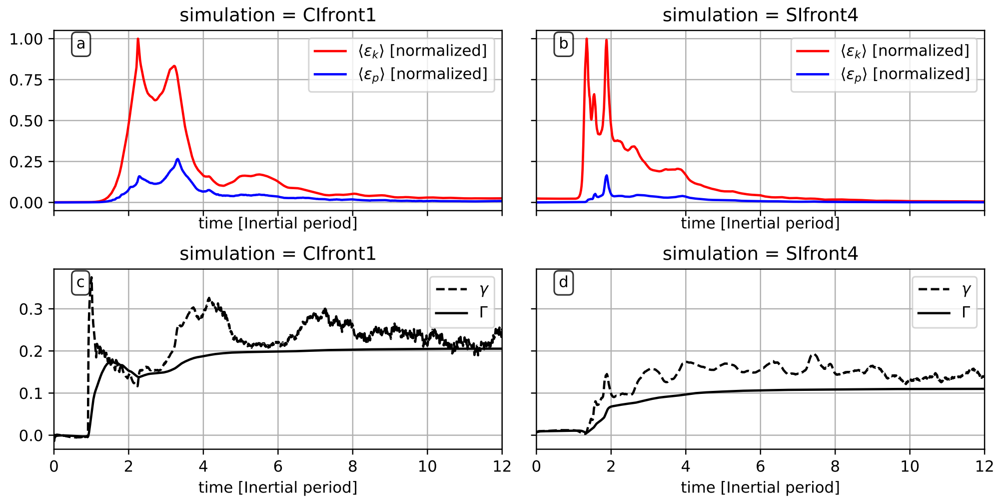

FIG. 3. Evolution of the dissipation and mixing efficiency metrics for simulations CIfront1 (left panel) and SIfront4 (right panels). $\langle \epsilon_k \rangle$ and $\langle \varepsilon_p \rangle$ are shown in panels a and b, instantaneous (γ, dashed lines) and cumulative (Γ, solid lines) mixing efficiencies are shown in panels c and d. The values of $\langle \epsilon_k \rangle$ and $\langle \varepsilon_p \rangle$ have been normalized by the maximum of $\langle \epsilon_k \rangle$ since the magnitudes of both in this case are domain-dependent.

this section and encourage readers to refer to the animations that are available in the Supporting Information to gain more intuition.

Results for these simulations are shown in Figure 3, where the upper panels show the kinetic energy dissipation rate and the mixing rate of buoyancy. After a quiescent start (indicated by low values of $\langle \varepsilon_k \rangle$ and $\langle \varepsilon_p \rangle$), primary CSIs (which are mostly 2D in the y-z plane) develop within 1 inertial period. Between 1 to 3 inertial periods the shear from the primary instabilities becomes sufficiently strong to generate secondary instabilities (see Section b) that mediate the transition to full 3D turbulence; this roughly coincides with the first peak in $\langle \varepsilon_k \rangle$. The ensuing turbulent flow can be seen in panels c-f of Figure 1. Note that simulation SIfront4 reaches the onset of turbulence earlier than simulation CIfront1 because it has lower values of $\hat{q}_b$ (see Figure 2), which translates into a faster growth rate for the CSIs per Equation (5) (Haine and Marshall 1998).

Internal waves are generated in all our simulations during the emergence of the secondary instabilities (which is explosive in nature). However the total amount of energy radiated via internal waves (as quantified by the energy dissipated in the sponge layers) is never larger than around 1/1000th of the kinetic energy dissipated by the instabilities, which qualitatively matches

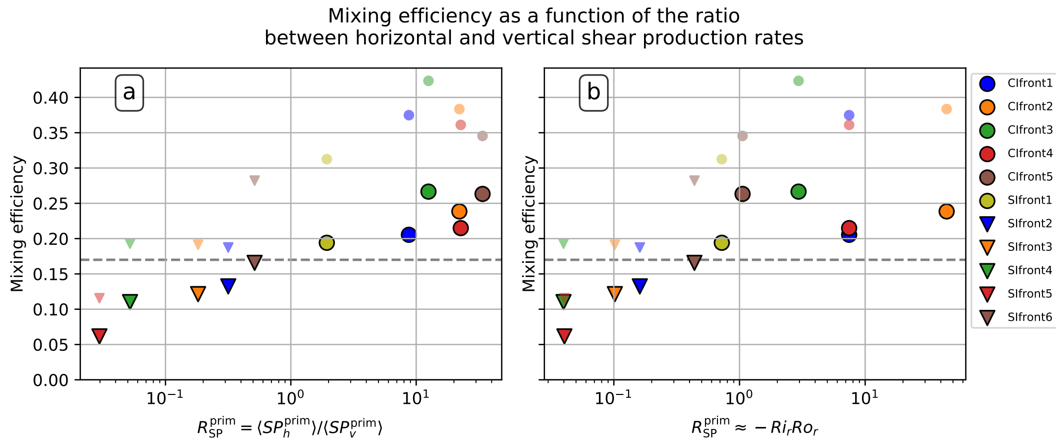

Fig. 4. Final cumulative mixing efficiency Γ_∞ (large bold circles) and maximum of the instantaneous mixing efficiency γ (small semi-transparent circles) as a function of the ratio between horizontal and vertical shear production rates. Centrifugally-dominated CSIs are the rightmost points in each panel while symmetrically-dominated CSIs are the leftmost points. Panel a shows a diagnostic measure of the ratio, while panel b shows an estimate based on Equation (2). The dashed gray line indicates the value of 0.17 for reference.

the findings of Kloosterziel et al. (2007) for centrifugal instabilities. Interestingly, more waves are visible on the lighter side of the front compared to the heavier side. This can be seen in panels c and d of Figure 1 (the portion of the domain shown does not include the sponge layers).

In Figure 3 panels c and d we show two measures of mixing efficiency: the instantaneous mixing efficiency γ (dashed lines) and the cumulative mixing efficiency Γ (solid lines). The pattern of the instantaneous measure is significantly noisier than the cumulative one, with abrupt changes in γ short times (this is especially true for simulation CIfront1). This variability suggests caution in extrapolating instantaneous mixing efficiencies from observations as a means of characterizing the integrated mixing of a given flow throughout its lifespan. For the purposes of our analysis, we overcome this limitation by using the cumulative mixing efficiency Γ (Equation (7)). As $t \to \infty$, $\Gamma(t)$ converges to a value Γ_∞, which we take to be representative of the total mixing of the flow. In practice a good approximation for Γ_∞ can be obtained by taking Γ at around 12 inertial periods (after its value has approximately converged in all our simulations), which we adopt as our approach.

We plot results for Γ_∞ in Figure 4 as a function of the ratio between the average horizontal and vertical shear production rates (results for Γ_∞ are the larger, bolder symbols). Figure 4a shows Γ_∞ as a function of a measure of the ratio of shear production rates $R_{\mathrm{SP}}^{\mathrm{prim}}$ (the calculations are detailed in Appendix a) and Figure 4b plots it as a function of an estimate of that quantity ($R_{\mathrm{SP}}^{\mathrm{prim}} \approx -Ro_r\, Ri_r$, from Equations (3)-(4)). Recall that small values of $R_{\mathrm{SP}}^{\mathrm{prim}}$, imply symmetrically-dominated the CSIs. In both Figures 4a-b there is a clear tendency of centrifugally-dominated CSIs ($R_{\mathrm{SP}} > 1$) to have higher mixing efficiencies than symmetrically-dominated ones. We also plot the maximum value of the instantaneous mixing efficiency, $\gamma_{\max}$, for each simulation as smaller symbols with slight transparency. The same pattern is evident, with the mixing efficiency increasing as the modes become more centrifugally dominated.

Figure 4 shows a clear pattern in which values of Γ_∞ for symmetrically-dominated CSIs ($R_{\mathrm{SP}}^{\mathrm{prim}} < 1$) are lower than the canonical value of 0.17 (shown as a dashed gray line for reference), while values for centrifugally-dominated CSIs ($R_{\mathrm{SP}}^{\mathrm{prim}} > 1$) are higher. Additionally, values of $\gamma_{\max}$ for centrifugally-dominated CSIs can reach even higher values. This large range of values in Figure 4 is in qualitative agreement with previous indications that mixing efficiencies of submesoscale CSIs can significantly deviate from the commonly-used value (Taylor and Ferrari 2010; Spingys et al. 2021).

We note that the mixing efficiencies found in these simulations are somewhat more moderate than those reported from 2D simulations using constant eddy viscosities, where it has been argued that centrifugal instabilities may generate $\gamma \approx 1$ (Jiao and Dewar 2015). We are able to reproduce similar results for our basic frontal configuration when using a similar 2D constant-viscosity set-up (ie. low Reynolds number direct numerical simulation, matching the simulations used in the study), however not when using LES closures and in 3D. Furthermore, even in 2D constant-viscosity simulations, using Γ as a metric (instead of γ) also indicates more moderate mixing efficiencies since the largest values of γ happen after most of the turbulence has dissipated (see e.g. Jiao and Dewar (2015, Figure 14)) and thus contributes little to the total mixing performed by the flow. These numerical results (and the connections to Kelvin-Helmholtz mixing discussed below) thus are taken to indicate that, while centrifugal instabilities generate significantly enhanced mixing efficiencies, some of the prior results indicating CSIs generating near perfectly efficient mixing may have been reflective of numerical methods, and not entirely representative of high-Reynolds number oceanic flows.

It is worth mentioning that the range of values for N_0^2 is significantly larger than the range of values of other parameters in our simulations (see Table 1). As such, changes in N_0^2 are responsible for

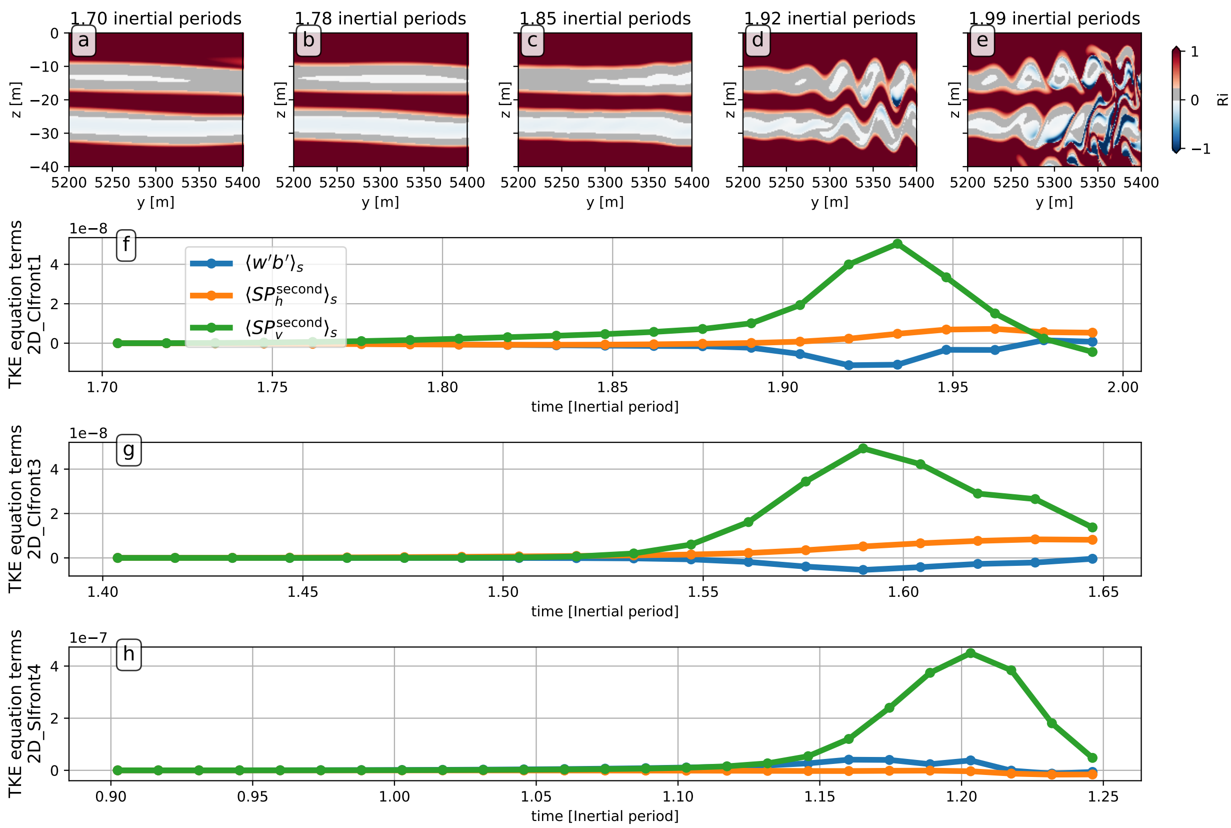

FIG. 5. Analysis of the secondary instability for simulation 2D_CIfront1, 2D_CIfront3 and 2D_SIfront4. First row of panels (a-e) shows the Richardson number Ri, with values between 0 and 0.25 shaded in gray, for Simulation 2D_CIfront1. Panel f shows the evolution of the subdomain averages (the subdomain being the one shown in panels a-e) of three different components of the TKE budget equation for Simulation 2D_CIfront1: buoyancy flux, shear production rate in the y-direction ($\langle SP_h^{\text{second}} \rangle_s$) and shear production rate in the z-direction ($\langle SP_v^{\text{second}} \rangle_s$). Panel g and h show the same subdomain averages for Simulations 2D_CIfront3 and 2D_SIsurfjet4. See Appendix b for details about the calculation of these averaged quantities.

most of the organization of points seen in Figure 4. While our set-up is such that large variations in N_0^2 are needed to cover the submesoscale range of the Ro_r-$1/Ri_r$ parameter space (without relying on unrealistic values of other parameters), this is not necessarily the case in the ocean. As such, while we expect the relation between the mixing efficiency and $Ri_r\, Ro_r$ to hold for more general cases (preliminary investigations with an interior jet geometry produced similar results), it may be the case that the Richardson number is the dominant factor for more general conditions. We leave this investigation for future studies.

b. The nature of the secondary instabilities

The variations in mixing efficiency across CSI simulations indicate changes in the mixing generated by secondary instabilities during the equilibration process. In this section we therefore identify the secondary instabilities that mediate the transition from CSI modes to full 3D turbulence. Previous work by Taylor and Ferrari (2009) has shown that pure symmetric instabilities (CSIs in the absence of any centrifugal modes) equilibrate via Kelvin-Helmholtz instabilities (KHIs). Griffiths (2003) likewise inferred KHIs as the equilibration mechanism for centrifugal instability, although this was based on simulations that did not directly resolve overturning motions.

A significant difference between centrifugal and symmetric instabilities — which might be hypothesized as the source of the enhanced mixing efficiencies — is that the fastest growing linear centrifugal modes cross isopycnals, whereas the symmetric modes do not (Thomas et al. 2013). This suggests the possibility that buoyancy advection by centrifugal instabilities adds a gravitational instability component to the equilibration process, which is known to have higher mixing efficiencies than KHIs (Gayen et al. 2013; Wykes and Dalziel 2014). Given the uncertainty in the equilibration mechanism of centrifugal instabilities, we therefore focus in this section on the onset of the secondary instabilities.

Thus, for the purposes of this section, we run three 2D simulations with a constant eddy diffusivity (2D_CIfront1, 2D_CIfront3 and 2D_SIfront4; see Table 2) that are otherwise identical to simulations CIfront1, CIfront3 and SIfront4. The use of a constant eddy diffusivity avoids possible artificial changes in the energetics and dynamics due to the subgrid-scale model (Piomelli et al. 1990), and the two-dimensionality is designed to save computational resources (since we anticipate both the primary and secondary instabilities to be 2D in the y-z plane (Peltier and Caulfield 2003; Rahmani et al. 2014)). We focus the analysis on a small portion of the domain (to avoid interference by the edges of CSI modes and other features of the flow) and quantify the horizontal and vertical shear production rates separately, as well as the buoyancy production rate and the Richardson number. The subdomains used, however, were verified to be representative of the turbulence transition of the CSI modes as a whole.

Results are shown in Figure 5a-f for the centrifugally-dominated Simulation 2D_CIfront1. The upper panels (a-e) show the evolution of Ri in snapshots as time progresses, with Ri values between 0 and 1/4 shaded gray in order to indicate areas that are susceptible to KHIs (Miles 1961; Howard

1961). It is clear in the first panels that a large horizontal portion of the subdomain is susceptible to KHIs as indicated by the gray-shaded areas. The light white-bluish areas indicate that a portion of the domain also has slightly negative Ri (their magnitudes are mostly smaller than 0.05), which is a consequence of the centrifugal modes crossing isopycnals, as expected. In panel d we see undulations qualitatively characteristic of KHIs before a decay into turbulence in panel e.

Panel f of Figure 5 shows subdomain means (denoted by $\langle \cdot \rangle_s$; the subdomain being the rectangular domain portion shown in the upper panels) of the vertical buoyancy flux and shear production rate components for Simulation 2D_CIfront1 (details about this calculation can be found in Appendix b). At early times, all the averages are approximately zero, but the secondary instability growth is dominated by vertical shear production. Note that the buoyancy production rate is actually negative (implying energy moving from kinetic form to potential form) despite portions of the subdomain having slightly unstable stratification. Thus, despite buoyancy advection generating regions potentially susceptible to gravitational instability, the primary energy source for the secondary instabilities remains vertical shear production. The same analysis applied to Simulation 2D_CIfront3 produces similar results (Figure 5g).

These characteristics are expected of KHIs (Peltier and Caulfield 2003), which strongly suggests that centrifugally-dominated CSIs equilibrate through secondary KHIs. The same analysis for symmetrically-dominated CSIs (using Simulation 2D_SIfront4 and shown in Figure 5g) produces very similar results (albeit with smaller regions of unstable stratification due to the alignment of the symmetric modes with isopycnals) and identical conclusions — consistent with earlier analysis by Taylor and Ferrari (2009). In order to make sure that this feature is not specific to our frontal setup, we ran the same analysis for a centrifugally-unstable interior jet similar to the one considered by Jiao and Dewar (2015), but with a higher resolution. The results (not shown) are again extremely similar to the ones just described. We therefore proceed with the assumption that CSIs in the submesoscale portion of the parameter space (regardless of being symmetrically- or centrifugally-dominated) equilibrate via KHIs that emerge from the vertical shear of the primary modes before the onset of gravitational instability.

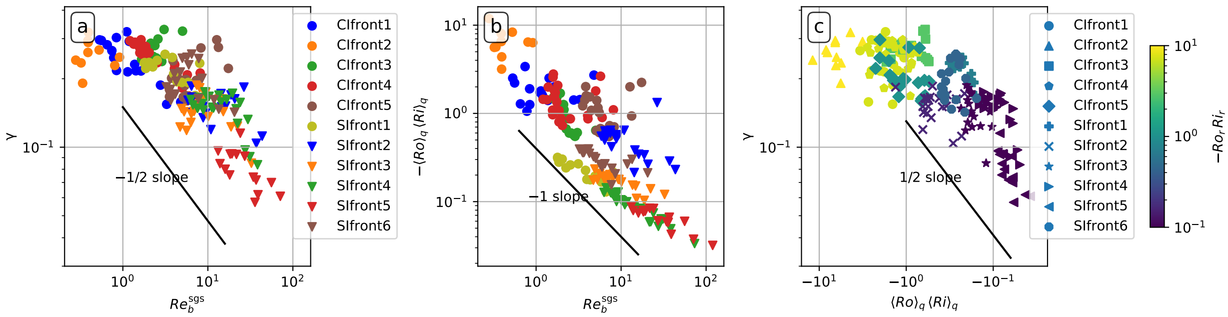

FIG. 6. Scatter plot of several quantities for all 3D simulations in this work. Each symbol is a different simulation. Panel a: instantaneous mixing efficiency γ as against Re_b^{sgs}. The solid black line indicates a slope of $\gamma \sim (Re_b^{\text{sgs}})^{-1/2}$ for reference. Panel b: $-\langle Ro\rangle_q \langle Ri\rangle_q$ (where $\langle\cdot\rangle_q$ denotes an average over the region where $\hat{q}_b < 0$ at $t = 0$) as a function of Re_b^{sgs}. The solid black line indicates a slope of $(Re_b^{\text{sgs}})^{-1}$ for reference. Panel c: instantaneous mixing efficiency γ plotted as a function of $\langle Ro\rangle_q \langle Ri\rangle_q$, with points colored according to the value $-Ro_r\, Ri_r$ of the simulation.

c. The role of the secondary instabilities in the mixing efficiency

Given that the transition to 3D turbulence is mediated by KHIs, it is now possible to connect these geophysical flows with some of the literature on turbulence in stratified flows. Many recent investigations focus on the buoyancy Reynolds number Re_b (Shih et al. 2005; Bouffard and Boegman 2013; Salehipour and Peltier 2015; Mashayek et al. 2017a) to explain the mixing efficiencies of overturning motions in stratified environments, which we found to be a good predictor of γ in our simulations. In experimental settings and in direct numerical simulations Re_b is well-defined, but it needs to be adapted for use with our large-eddy simulations, where the eddy viscosity varies in time and space. We thus define the subgrid-scale buoyancy Reynolds number as

$$Re_b^{\text{sgs}} = \frac{\langle \varepsilon_k \rangle_q}{\langle \nu_e \rangle_q N_0^2}, \tag{17}$$

where ν_e is the eddy viscosity and $\langle\cdot\rangle_q$ denotes an average over the region where $\hat{q}_b < 0$ at $t = 0$[1]. In principle any consistent averaging procedure can be use to define Re_b^{sgs}, but we choose $\langle\cdot\rangle_q$ due to the changing distribution of unstable areas in our set-up across the parameter space (see for example the panels a and b of Figure 1). We chose to use N_0^2 here instead of $\langle db/dz\rangle_q$ since we

[1]Note that $\langle\cdot\rangle_q$ is different from the previously-introduced $\langle\cdot\rangle$ and $\langle\cdot\rangle_s$, which denote an average over the whole domain and an average over the rectangular subdomain shown in Figures 5a-e, respectively.

want to characterize the background stratification against which the overturning motions need to do work without the influence of the locally unstable stratification generated by the overturning motions themselves. Results change only slightly when evaluating using $\langle db/dz \rangle_q$.

A necessary note is that previous studies investigating Re_b rely on very idealized (and therefore very well-controlled) numerical simulations, where turbulent regions are more easily identified and averaging procedures can be performed in a straightforward manner. This is not the case for our simulations, which are significantly more realistic, contributing to a less predictable pattern of turbulence. As a result, turbulence in our simulations happens in patches (see panels e-f of Figure 1, which shows ε_k), which is more representative of real ocean turbulence, but also complicates comparisons of buoyancy Reynolds magnitude with idealized studies and between different datasets (Mashayek et al. 2017b; Howland et al. 2020; Caulfield 2021) — see also discussion in Mashayek et al. (2021, Section 7). Thus, we refrain from comparing absolute values of Re_b^{sgs} directly with Re_b from the literature and focus on the variations of γ with buoyancy Reynolds number instead.

Similar to previous studies (Shih et al. 2005; Salehipour and Peltier 2015), we compare instantaneous mixing efficiencies γ with instantaneous values of Re_b^{sgs} in Figure 6a. In order to ensure that only cases with significant 3D turbulence were taken into account, we only consider times after the peak in the dissipation rate $\langle \varepsilon_k \rangle$ (indicating a transition to full 3D turbulence) and discard points where $\langle \varepsilon_k \rangle_q$ is smaller than $1 \times 10^{-10}\,\mathrm{m}^2/\mathrm{s}^3$. Figure 6a show a pattern where, for small values of Re_b^{sgs}, γ does not depend on Re_b^{sgs}, followed by a power-law dependence for larger values which follows a $-1/2$ slope (as evidenced by comparing it with the solid line). Both the region of approximately-constant γ for small Re_b^{sgs} and the region of power-law dependence match well with previous findings for KHI (Shih et al. 2005; Lozovatsky and Fernando 2013; Salehipour and Peltier 2015); a result that is robust in our simulations to different averaging procedures.

The agreement between our data and simulations of idealized KHIs is evidence that the mixing efficiencies of these submesoscale instabilities are ultimately controlled by the small-scale overturning motions of the flows that emerge as a consequence of CSIs. This suggests that CSIs control the mixing efficiency by adjusting the background for KHIs to emerge: namely the stratification, vertical shear and dissipation rate, which directly modulate the Richardson and buoyancy Reynolds numbers. Along with the Prandtl number, this sets all three nondimensional parameters necessary to characterize overturning motions in stratified flow (Mashayek et al. 2017a, Section 2.2) — if the kinetic energy is included, a Froude number is also necessary (Caulfield 2021, Section 2.4), which can also be controlled by CSIs. We note that, although some authors have found the Froude number Fr to be preferred for organizing mixing efficiency results (Maffioli et al. 2016; Garanaik and Venayagamoorthy 2019), we found no Froude number dependence for the mixing efficiency in our results.

We further find an inverse relation between Re_b^{sgs} and $-\langle Ro\rangle_q\langle Ri\rangle_q$ in our simulations, shown in Figure 6b, such that

$$-\langle Ro\rangle_q\langle Ri\rangle_q \sim (Re_b^{\mathrm{sgs}})^{-1}$$

(solid black line in panel b). This result can explain the pattern of mixing efficiencies seen in Figure 4, where symmetrically-dominated CSIs (where $-\langle Ro\rangle_q\langle Ri\rangle_q < 1$) tend to have higher buoyancy Reynolds number than centrifugally-dominated CSIs (where $-\langle Ro\rangle_q\langle Ri\rangle_q > 1$). This relation can be used to plot γ as a function of $\langle Ro\rangle_q\langle Ri\rangle_q$ in Figure 6c, where we also see that points collapse rather well. This comparison is similar to that in Figure 4, and we see that the result again indicates that centrifugally-dominated CSIs tend towards higher values of γ, and the opposite for symmetrically-dominated CSIs.

We note that the collapse of points in Figure 6b could be explained by the fact that N_0^2 spans a much larger range of values in our simulations than other parameters and dominates the modulation of the product $Ri_r\, Ro_r$. It thus remains to be seen if the organization of points seen in Figure 6b,c is a general feature of oceanic flows, or if it emerges due to characteristics of frontal flow geometries. Although we note that preliminary results with an interior jet set-up match Figure 4b reasonably well.

5. Discussion and conclusion

We have used LES to investigate several geophysical flows that are unstable to submesoscale centrifugal-symmetric instabilities (CSIs) with the main goal of systematically examining their mixing efficiencies. All simulations in this paper follow a similar evolution: primary CSIs quickly develop in the domain, increase the vertical shear, which prompts the emergence of secondary instabilities (which we showed to be Kelvin-Helmholtz instabilities, KHIs) that mediate the transition to small-scale turbulence, which ultimately dissipates kinetic energy and mixes buoyancy.

We showed that CSIs can generate a wide-range of mixing efficiencies ($0.05 \leq \Gamma_\infty \leq 0.3$), which can depart significantly from the community-standard value of 0.17 (Gregg et al. 2018; Caulfield 2021), suggesting caution in the use of a single mixing efficiency value for parameterizations where submesoscale turbulence is active. This variation in mixing efficiency is shown to be a consequence of the submesoscale, with centrifugally-dominated CSIs tending to have higher instantaneous and cumulative mixing efficiencies than symmetrically-dominated instabilities (see Figure 4). This pattern of mixing efficiencies due to CSIs can be well reproduced using only the Richardson and Rossby numbers ($Ri_r\, Ro_r$; Figure 4), suggesting a potential strategy for improving parameterized estimates of mixing due to submesoscale instabilities.

In all simulations considered here KHIs mediate the transition to turbulence, allowing us to explain the observed patterns in mixing efficiency by leveraging results from the stratified turbulence literature. Specifically, we show that variations in mixing efficiency can be understood as the result of CSIs setting the background state on which KHIs grow. CSIs modulate the strength of vertical shear, stratification, and turbulence intensity which have been shown to influence the mixing efficiency of KHIs through the Richardson and buoyancy Reynolds numbers (along with the Prandtl number (Mashayek et al. 2017a; Caulfield 2021)). Notably, we were able to reproduce the dependency of the instantaneous mixing efficiency γ on the buoyancy Reynolds number Re_b^{sgs} (adapted here for use with LES), shown in Figure 6a. The satisfactory collapse of points reproducing a result that is well-known in the stratified turbulence literature is evidence that these small overturning instabilities are what ultimately sets the mixing efficiency, providing a direct connection between submesoscale dynamical processes and stratified turbulence. We believe this to be one of the primary contributions of this paper, since it is likely that this control mechanism for CSIs extends beyond the portion of the parameter space explored here, providing the community with extra tools to analyze observations and develop parameterizations.

These results provide a potential explanation of recent observational findings of elevated mixing efficiencies in conditions susceptible to centrifugally-dominated CSI in the Orkney deep (Garabato et al. 2019; Spingys et al. 2021), as well as low mixing efficiencies in simulations of forced-symmetric instability in the surface boundary layer where the stratification remains small (Taylor and Ferrari 2010). We note however that, despite this qualitative agreement, we do not find mixing efficiencies as large as implied by some previous work on CSIs (Spingys et al. 2021). This may be a result of the uncertainty in observational estimates, or that the mixing efficiency of CSIs can vary over an even wider range as a consequence of other parameters or flow geometries not varied here. For example, in weak fronts with $Ro_b \approx 0$ and shallow isopycnal slopes, CSIs can grow by extracting potential energy from the balanced flow (Wienkers et al. 2021), potentially introducing a gravitational component to the energetics that may contribute to higher rates of buoyancy mixing. However, to the extent that our finding of KHIs mediating the transition to turbulence is general for CSIs, we expect our results to be robust, as they depend on the local background state felt by the growing KHI modes, and not directly on the geometry or parameters at the submesoscale.

Finally, evidence that CSIs are common in both the surface and bottom boundary layer suggests the variations in mixing efficiency shown here may be an important aspect of larger-scale ocean dynamics and circulation (Allen and Newberger 1998; Taylor and Ferrari 2010; D'Asaro et al. 2011; Thomas et al. 2013; Gula et al. 2016a; Savelyev et al. 2018; Dewar et al. 2015; Molemaker et al. 2015; Gula et al. 2016b; Garabato et al. 2019; Wenegrat et al. 2018a; Wenegrat and Thomas 2020). The case of abyssal flows offers a particularly compelling example, as observations suggest the possibility of CSIs generated by flow along bottom topography (Ruan et al. 2017; Garabato et al. 2019; Spingys et al. 2021). Centrifugally-dominated instabilities — generated preferentially in regions of steep slopes and strong stratification (Wenegrat et al. 2018a) — in particular provide a route for the efficient mixing of buoyancy, and hence may contribute to abyssal watermass transformation, a key component of the global overturning circulation. Quantification of the integrated effect of CSIs in both the surface and bottom boundary layer, and the variations of mixing efficiency documented here, remains an open target for future study.

Acknowledgments. T.C. and J.O.W. were supported by the National Science Foundation grant number OCE-1948953. We would also like to acknowledge high-performance computing support from Cheyenne (doi:10.5065/D6RX99HX) provided by NCAR's Computational and Information Systems Laboratory, sponsored by the National Science Foundation.

APPENDIX

A1. Calculation of the rate of irreversible mixing of buoyancy

We calculate the irreversible mixing of buoyancy based on the theory of Winters et al. (1995). An evolution equation for background potential energy for a control volume can be written as (Winters et al. 1995)

$$\frac{d}{dt}\langle E_b \rangle = S_{\text{adv}} + S_{\text{diff}} + \langle \varepsilon_p \rangle, \tag{A1}$$

where $\langle E_b \rangle$ is the average background potential energy (the portion of the potential energy unavailable for conversion into kinetic form) per unit mass, S_{adv} and S_{diff} are the advective and diffusive fluxes of $\langle E_b \rangle$ across the volume's boundaries. The sponge layers used in our simulations do not directly modify the buoyancy, so they do not appear in Equation (A1). $\langle \varepsilon_p \rangle$ is the average irreversible mixing of buoyancy (due to diapycnal mixing within the control volume), and it appears as a non-negative rate of change in Equation (A1) because potential energy lost due to internal mixing is irreversibly stored as background potential energy (Winters et al. 1995; Winters and D'Asaro 1996).

The term S_{adv} is identically zero for our simulations due to the boundary conditions. S_{diff} on the other hand is nonzero for our domain but its effect on $\langle E_b \rangle$ was found to be negligibly small. Thus we assume $S_{\text{diff}} \approx 0$. This allows us to simplify Equation (A1), leading to our equation for $\langle \varepsilon_p \rangle$

$$\langle \varepsilon_p \rangle = \frac{d}{dt}\langle E_b \rangle, \tag{A2}$$

which is similar to Equation (18) of Winters et al. (1995).

Thus, in order to apply Equation (A2), we estimate $\langle E_b \rangle$ by adiabatically sorting the buoyancy field b at every time step to arrive at a reference state that minimizes horizontal buoyancy gradients (Winters et al. 1995). Although this approximation is the main source of error in our calculation of $\langle \varepsilon_p \rangle$, we found that the error is small enough to be neglected.

A2. Calculation of the shear production terms

a. Shear production terms for the primary instabilities

The general definition of the shear production terms comes from the turbulent kinetic energy prognostic equation and reads

$$SP_j = -u_i' u_j' \frac{\partial}{\partial x_j} U_i, \tag{A3}$$

where $U_j = (U, V, W)$ is a Reynolds-averaged velocity vector about which the turbulent fluctuations u_i' are calculated, and summation is implied for the i index only (Stull 1988). In this case we want to consider the rate at which shear of the average flow transfers energy to the primary instabilities; namely the CSIs. Thus, the fluctuations u_i' should ideally capture the CSIs only.

Given the nature of our set-up, this is challenging to achieve with directional averages (recall that CSIs are mainly 2D in nature, so even averaging in the x-direction would not achieve this result). Hence we consider an ensemble average over many realizations of this flow and make the assumption that such an average of the flow velocities is well approximated by the flow velocities at the initial condition. We then approximate U_j as the flow velocities at the initial condition (given by Equations (9)–(14)), simplify Equation (A3) accordingly, and define horizontal and vertical shear production rate terms for the primary instabilities as

$$SP_h^{\text{prim}} = -u'v' \frac{\partial U}{\partial y} \tag{A4}$$

$$SP_v^{\text{prim}} = -u'w' \frac{\partial U}{\partial z}. \tag{A5}$$

According to this definition the shear production rate is zero at $t = 0$ and starts to evolve as the instabilities start to develop. We quantify the value of the shear production rate terms at a time $t = 15/\omega_{\max}$, where $\omega_{\max}$ is the maximum growth rate for CSIs (Equation 5). This choice of time captures a well-developed CSI before the onset of full 3D turbulence. Different choices of time were investigated (including some based not on $\omega_{\max}$ but on the evolution of $\langle \varepsilon_k \rangle$) and the results were found to be robust.

b. Shear production terms for the secondary instabilities

For this section, the purpose of the analysis is to capture the rate of energy input into the secondary instabilities by the CSIs. Ideally, it is then necessary to capture only the secondary instabilities in the fluctuation terms u_i', and the background flow (with the CSIs) should be captured in the U_j terms. Similarly to the primary instabilities analysis, the best approach we found is to consider an ensemble average that we assume to be well approximated by the state of the flow at a time $t = t_1$ in which the primary instabilities are well-developed, but the secondary instabilities still have not started emerging. This choice is done manually, since a programmatic way to choose t_1 consistently across simulations could not be found. We found, however, that the precise choice of time does not alter the results significantly as long as the two aforementioned criteria are observed and as long as we consider a portion of the domain that isolates the emergence of secondary instabilities.

For these calculations $U_j = (U, V, W) \neq 0$ (since they correspond to CSIs), and for a 2.5D set-up (without an x-direction) we can define these shear production rate terms for the secondary instabilities as

$$SP_h^{\text{second}} = -u'v'\frac{\partial U}{\partial y} - v'^2\frac{\partial V}{\partial y} - w'v'\frac{\partial W}{\partial y} \tag{A6}$$

$$SP_v^{\text{second}} = -u'w'\frac{\partial U}{\partial z} - v'w'\frac{\partial V}{\partial z} - w'^2\frac{\partial W}{\partial z}. \tag{A7}$$

References

Allen, J., and P. Newberger, 1998: On symmetric instabilities in oceanic bottom boundary layers. *Journal of physical oceanography*, **28 (6)**, 1131–1151.

Bluteau, C., N. Jones, and G. Ivey, 2013: Turbulent mixing efficiency at an energetic ocean site. *Journal of Geophysical Research: Oceans*, **118 (9)**, 4662–4672.

Bouffard, D., and L. Boegman, 2013: A diapycnal diffusivity model for stratified environmental flows. *Dynamics of Atmospheres and Oceans*, **61**, 14–34.

Buckingham, C. E., N. S. Lucas, S. E. Belcher, T. P. Rippeth, A. L. Grant, J. Le Sommer, A. O. Ajayi, and A. C. Naveira Garabato, 2019: The contribution of surface and submesoscale processes to turbulence in the open ocean surface boundary layer. *Journal of Advances in Modeling Earth Systems*, **11 (12)**, 4066–4094.

Caulfield, C., 2021: Layering, instabilities, and mixing in turbulent stratified flows. *Annual Review of Fluid Mechanics*, **53**, 113–145.

D'Asaro, E., C. Lee, L. Rainville, R. Harcourt, and L. Thomas, 2011: Enhanced turbulence and energy dissipation at ocean fronts. *science*, **332 (6027)**, 318–322.

De Lavergne, C., G. Madec, J. Le Sommer, A. G. Nurser, and A. C. N. Garabato, 2016: The impact of a variable mixing efficiency on the abyssal overturning. *Journal of Physical Oceanography*, **46 (2)**, 663–681.

Dewar, W., J. McWilliams, and M. Molemaker, 2015: Centrifugal instability and mixing in the california undercurrent. *Journal of Physical Oceanography*, **45 (5)**, 1224–1241.

Garabato, A. C. N., and Coauthors, 2019: Rapid mixing and exchange of deep-ocean waters in an abyssal boundary current. *Proceedings of the National Academy of Sciences*, **116 (27)**, 13 233–13 238.

Garanaik, A., and S. K. Venayagamoorthy, 2019: On the inference of the state of turbulence and mixing efficiency in stably stratified flows. *Journal of Fluid Mechanics*, **867**, 323–333.

Gayen, B., G. O. Hughes, and R. W. Griffiths, 2013: Completing the mechanical energy pathways in turbulent rayleigh-bénard convection. *Physical review letters*, **111 (12)**, 124 301.

Gregg, M. C., E. A. D'Asaro, J. J. Riley, and E. Kunze, 2018: Mixing efficiency in the ocean. *Annual review of marine science*, **10**, 443–473.

Griffiths, S. D., 2003: Nonlinear vertical scale selection in equatorial inertial instability. *Journal of the atmospheric sciences*, **60 (7)**, 977–990.

Gula, J., M. J. Molemaker, and J. C. McWilliams, 2016a: Submesoscale dynamics of a gulf stream frontal eddy in the south atlantic bight. *Journal of Physical Oceanography*, **46 (1)**, 305–325.

Gula, J., M. J. Molemaker, and J. C. McWilliams, 2016b: Topographic generation of submesoscale centrifugal instability and energy dissipation. *Nature communications*, **7 (1)**, 1–7.

Haine, T. W., and J. Marshall, 1998: Gravitational, symmetric, and baroclinic instability of the ocean mixed layer. *Journal of physical oceanography*, **28 (4)**, 634–658.

Howard, L. N., 1961: Note on a paper of john w. miles. *Journal of Fluid Mechanics*, **10 (4)**, 509–512.

Howland, C. J., J. R. Taylor, and C. Caulfield, 2020: Mixing in forced stratified turbulence and its dependence on large-scale forcing. *Journal of Fluid Mechanics*, **898**.

Jiao, Y., and W. Dewar, 2015: The energetics of centrifugal instability. *Journal of Physical Oceanography*, **45 (6)**, 1554–1573.

Kämpf, J., 2010: *2.5D Vertical Slice Modelling*, 97–124. Springer Berlin Heidelberg, Berlin, Heidelberg, https://doi.org/10.1007/978-3-642-10610-1_4.

Kloosterziel, R., G. Carnevale, and P. Orlandi, 2007: Inertial instability in rotating and stratified fluids: barotropic vortices. *Journal of Fluid Mechanics*, **583**, 379–412.

Lévy, M., P. J. Franks, and K. S. Smith, 2018: The role of submesoscale currents in structuring marine ecosystems. *Nature communications*, **9 (1)**, 1–16.

Lilly, D. K., 1962: On the numerical simulation of buoyant convection. *Tellus*, **14 (2)**, 148–172, https://doi.org/https://doi.org/10.1111/j.2153-3490.1962.tb00128.x.

Lozovatsky, I., and H. Fernando, 2013: Mixing efficiency in natural flows. *Philosophical Transactions of the Royal Society A: Mathematical, Physical and Engineering Sciences*, **371 (1982)**, 20120 213.

Maffioli, A., G. Brethouwer, and E. Lindborg, 2016: Mixing efficiency in stratified turbulence. *Journal of Fluid Mechanics*, **794**.

Marshall, J., A. Adcroft, C. Hill, L. Perelman, and C. Heisey, 1997: A finite-volume, incompressible navier stokes model for studies of the ocean on parallel computers. *Journal of Geophysical Research: Oceans*, **102 (C3)**, 5753–5766, https://doi.org/https://doi.org/10.1029/96JC02775.

Mashayek, A., C. Caulfield, and M. Alford, 2021: Goldilocks mixing in oceanic shear-induced turbulent overturns. *Journal of Fluid Mechanics*, **928**, https://doi.org/10.1017/jfm.2021.740.

Mashayek, A., C.-c. P. Caulfield, and W. Peltier, 2017a: Role of overturns in optimal mixing in stratified mixing layers. *Journal of Fluid Mechanics*, **826**, 522–552.

Mashayek, A., H. Salehipour, D. Bouffard, C. Caulfield, R. Ferrari, M. Nikurashin, W. Peltier, and W. Smyth, 2017b: Efficiency of turbulent mixing in the abyssal ocean circulation. *Geophysical Research Letters*, **44 (12)**, 6296–6306.

McWilliams, J. C., 2016: Submesoscale currents in the ocean. *Proceedings of the Royal Society A: Mathematical, Physical and Engineering Sciences*, **472 (2189)**, 20160 117.

Miles, J. W., 1961: On the stability of heterogeneous shear flows. *Journal of Fluid Mechanics*, **10 (4)**, 496–508.

Molemaker, M. J., J. C. McWilliams, and W. K. Dewar, 2015: Submesoscale instability and generation of mesoscale anticyclones near a separation of the california undercurrent. *Journal of Physical Oceanography*, **45 (3)**, 613–629.

Moum, J. N., 1996: Efficiency of mixing in the main thermocline. *Journal of Geophysical Research: Oceans*, **101 (C5)**, 12 057–12 069.

Osborn, T., 1980: Estimates of the local rate of vertical diffusion from dissipation measurements. *Journal of physical oceanography*, **10 (1)**, 83–89.

Peltier, W., and C. Caulfield, 2003: Mixing efficiency in stratified shear flows. *Annual review of fluid mechanics*, **35 (1)**, 135–167.

Piomelli, U., T. A. Zang, C. G. Speziale, and M. Y. Hussaini, 1990: On the large-eddy simulation of transitional wall-bounded flows. *Physics of Fluids A: Fluid Dynamics*, **2 (2)**, 257–265.

Rahmani, M., G. Lawrence, and B. Seymour, 2014: The effect of reynolds number on mixing in kelvin–helmholtz billows. *Journal of fluid mechanics*, **759**, 612–641.

Ramadhan, A., and Coauthors, 2020: Oceananigans.jl: Fast and friendly geophysical fluid dynamics on GPUs. *Journal of Open Source Software*, **5 (53)**, 2018.

Ruan, X., A. F. Thompson, M. M. Flexas, and J. Sprintall, 2017: Contribution of topographically generated submesoscale turbulence to southern ocean overturning. *Nature Geoscience*, **10 (11)**, 840–845.

Salehipour, H., and W. Peltier, 2015: Diapycnal diffusivity, turbulent prandtl number and mixing efficiency in boussinesq stratified turbulence. *Journal of Fluid Mechanics*, **775**, 464–500.

Savelyev, I., and Coauthors, 2018: Aerial observations of symmetric instability at the north wall of the gulf stream. *Geophysical Research Letters*, **45 (1)**, 236–244.

Shih, L. H., J. R. Koseff, G. N. Ivey, and J. H. Ferziger, 2005: Parameterization of turbulent fluxes and scales using homogeneous sheared stably stratified turbulence simulations. *Journal of Fluid Mechanics*, **525**, 193–214.

Smagorinsky, J., 1963: General circulation experiments with the primitive equations: I. the basic experiment. *Monthly Weather Review*, **91 (3)**, 99 – 164, https://doi.org/10.1175/1520-0493(1963)091<0099:GCEWTP>2.3.CO;2.

Spingys, C. P., A. C. Naveira Garabato, S. Legg, K. L. Polzin, E. P. Abrahamsen, C. E. Buckingham, A. Forryan, and E. E. Frajka-Williams, 2021: Mixing and transformation in a deep western boundary current: A case study. *Journal of Physical Oceanography*, **51 (4)**, 1205–1222.

Stull, R. B., 1988: *An introduction to boundary layer meteorology*, Vol. 13. Springer Science & Business Media.

Taylor, J. R., and R. Ferrari, 2009: On the equilibration of a symmetrically unstable front via a secondary shear instability. *Journal of Fluid Mechanics*, **622**, 103–113.

Taylor, J. R., and R. Ferrari, 2010: Buoyancy and wind-driven convection at mixed layer density fronts. *Journal of Physical Oceanography*, **40 (6)**, 1222–1242.

Thomas, L. N., J. R. Taylor, R. Ferrari, and T. M. Joyce, 2013: Symmetric instability in the gulf stream. *Deep Sea Research Part II: Topical Studies in Oceanography*, **91**, 96–110.

Vreugdenhil, C. A., and J. R. Taylor, 2018: Large-eddy simulations of stratified plane couette flow using the anisotropic minimum-dissipation model. *Physics of Fluids*, **30 (8)**, 085 104, https://doi.org/10.1063/1.5037039.

Wenegrat, J. O., J. Callies, and L. N. Thomas, 2018a: Submesoscale baroclinic instability in the bottom boundary layer. *Journal of Physical Oceanography*, **48 (11)**, 2571–2592.

Wenegrat, J. O., and L. N. Thomas, 2020: Centrifugal and symmetric instability during ekman adjustment of the bottom boundary layer. *Journal of Physical Oceanography*, **50 (6)**, 1793–1812.

Wenegrat, J. O., L. N. Thomas, J. Gula, and J. C. McWilliams, 2018b: Effects of the submesoscale on the potential vorticity budget of ocean mode waters. *Journal of Physical Oceanography*, **48 (9)**, 2141–2165.

Wienkers, A., L. Thomas, and J. Taylor, 2021: The influence of front strength on the development and equilibration of symmetric instability. Part 1. Growth and saturation. *Journal of Fluid Mechanics*, **926**, https://doi.org/10.1017/jfm.2021.680.

Winters, K. B., and E. A. D'Asaro, 1996: Diascalar flux and the rate of fluid mixing. *Journal of Fluid Mechanics*, **317**, 179–193.

Winters, K. B., P. N. Lombard, J. J. Riley, and E. A. D'Asaro, 1995: Available potential energy and mixing in density-stratified fluids. *Journal of Fluid Mechanics*, **289**, 115–128.

Wunsch, C., and R. Ferrari, 2004: Vertical mixing, energy, and the general circulation of the oceans. *Annu. Rev. Fluid Mech.*, **36**, 281–314.

Wykes, M. S. D., and S. B. Dalziel, 2014: Efficient mixing in stratified flows: experimental study of a rayleigh–taylor unstable interface within an otherwise stable stratification. *Journal of fluid mechanics*, **756**, 1027–1057.